

Fabrication of Zinc Ferrite Nanocrystals by Sonochemical Emulsification and Evaporation: Observation of Magnetization and Its Relaxation at Low Temperature

Manickam Sivakumar,^{*,†,‡} Tsuyoshi Takami,[§] Hiroshi Ikuta,[§] Atsuya Towata,[†] Kyuichi Yasui,[†] Toru Tuziuti,[†] Teruyuki Kozuka,[†] Dipten Bhattacharya,^{||} and Yasuo Iida[†]

Ultrasonic Processing Group, Advanced Manufacturing Research Institute (AMRI), National Institute of Advanced Industrial Science and Technology (AIST), 2266-98 Anagahora, Shimoshidami, Moriyama-ku, Nagoya 463-8560, Japan, Department of Pharmaceutical Engineering & Technology, Bharathidasan Institute of Technology, Bharathidasan University, Tiruchirappalli 620024, India, Department of Crystalline Materials Science, Nagoya University, Furo-cho, Chikusa-ku, Nagoya 464-8603, Japan, and Electroceramics Division, Central Glass and Ceramic Research Institute, Calcutta 700 032, India

Received: September 6, 2005; In Final Form: June 3, 2006

A new ultrasound assisted emulsion (consisting of rapeseed oil and aqueous solution of Zn^{2+} and Fe^{2+} acetates) and evaporation protocol has been developed for the synthesis of zinc ferrite (ZnFe_2O_4) nanoparticles with narrow size distribution. The as-synthesized sample consisted of crystalline zinc ferrite particles with an average diameter of ~ 4 nm, whereas the average size of the heat-treated ferrite particles increases to ~ 12 nm. To remove the small amount of oil present on the surface of the as-synthesized ferrite sample, heat treatment was carried out at 350°C for 3 h. The as-synthesized and heat-treated ferrites were characterized by X-ray diffraction (XRD), infrared spectroscopy (IR), TGA/DTA, transmission electron microscopy (TEM), and energy dispersion X-ray spectroscopy (EDS) techniques. Magnetic measurements show that the nanocrystalline ZnFe_2O_4 , prepared through this technique, is either at par with those obtained in other cases or even more improved. Both the as-synthesized and heat-treated samples reveal relaxation of magnetization. Our study also shows that one can tailor the magnetization and relaxation pattern by suitably controlling the particle size of the nanocrystalline ZnFe_2O_4 . The key features of this method are avoiding (a) the cumbersome conditions that exist in the conventional methods, (b) the usage of necessary additive components (stabilizers or surfactants, precipitants), and (c) calcination requirements. In addition, rapeseed oil has replaced organic nonpolar solvents used in earlier studies. As a whole, this simple straightforward sonochemical approach results in a better pure phase system of nanoferrite with improved magnetic properties.

Introduction

In recent years, there has been tremendous activity for the preparation of transition metal ferrites with the molecular formula MFe_2O_4 , as they represent an important class of technological materials. Although these types of ferrites are traditionally prepared in bulk, the miniaturization of magnetic and electronic devices demands advanced materials with smaller sizes and new forms and shapes, such as nanoparticles.¹ Particularly, zinc ferrite (ZnFe_2O_4) nanoparticles have generated a lot of interest owing to their potential applications in gas sensor and semiconductor photocatalysis as their magnetic properties differ markedly from those of their bulk counterpart. Zinc ferrite has a normal spinel structure with tetrahedral A-sites occupied by Zn^{2+} ions and octahedral B-sites by Fe^{3+} ions.² It has been indicated that with the change in particle size ZnFe_2O_4 exhibits improved properties.^{3–7}

The ferrites with normal and inverse spinel structure exhibit a variety of magnetic order and properties depending on the choice of the tetrahedral A-site ion. For the nonmagnetic Zn ion at the tetrahedral site, the magnetic interaction takes place

only within octahedral B sites. It has been observed that bulk ZnFe_2O_4 depicts a long range order below 10 K as well as a short range order at higher temperature.⁸ On the other hand, $(\text{Ni,Zn})\text{Fe}_2\text{O}_4$ exhibits ferrimagnetic order, as a result of competition among A–A, A–B, and B–B exchange interactions. The saturation magnetization (M_s) for the bulk $(\text{Ni,Zn})\text{Fe}_2\text{O}_4$ system is found to be ~ 119 emu/g at ~ 10 K and ~ 70.3 emu/g at ~ 300 K.⁹ The size reduction down to nanometer scale can give rise to novel magnetic properties.¹⁰ Several studies^{1,11–15} have been carried out on nanocrystalline ferrites, both with magnetic and nonmagnetic ions at the A site, prepared by different techniques like sol–gel, coprecipitation, microemulsion, normal and reverse micelle, microwave, plasma, etc. In the case of nonmagnetic ion, Zn at the A site, it has been observed that for the particles of sizes of 3–6 nm the saturation magnetization at 3–10 K varies between 10 and 30 emu/g, whereas the coercive field (H_c) varies over 310–650 Oe. These observations have motivated us to carry out the magnetic hysteresis measurements at different temperatures between 5 and 300 K as well as field-cooled (f_c) and zero-field cooled (zfc) magnetization vs temperature measurements under different fields on as-synthesized and heat-treated nanocrystals of ZnFe_2O_4 prepared by the present sonochemical technique. These data help in understanding and comparing the nature of magnetic order in the as-synthesized nanocrystalline ZnFe_2O_4 and heat-treated system. In addition, we have studied the relaxation patterns of

* To whom correspondence should be addressed. E-mail: manickam-sivakumar@aist.go.jp. Fax: +81-52-7367400.

[†] Advanced Manufacturing Research Institute (AMRI).

[‡] Bharathidasan University.

[§] Nagoya University.

^{||} Central Glass and Ceramic Research Institute.

the magnetization at low temperature over a long time scale in order to shed light on the process of magnetization and its relaxation in both systems.

Several methods have been used for the preparation of this nanomagnetic ferrite system such as coprecipitation,^{16–18} microemulsion,¹⁹ sol–gel processing,²⁰ hydrothermal synthesis,^{21,22} thermal plasma synthesis,²³ and high energy ball milling.²⁴ Although these methods allow for the preparation of this ferrite, in most cases, they present several critical shortcomings.²⁵ To overcome the problems of these conventional methods, the development of new synthesis strategies has received increased attention in recent years.

Ultrasonic cavitation chemistry, an approach for synthesizing a wide variety of compounds at milder conditions is a rapidly developing method in materials research. The major advantage of this new method is that it offers a reliable and facile route for the control of both the synthetic process as well as the properties of the end product. This process, in fact, provides chemical homogeneity and reactivity through atomic level mixing within the precursor system, and pure phase crystalline materials can be prepared by annealing at reduced temperatures.²⁶ Sonochemical synthesis is a novel method for the production of nanosized materials. Using the sonochemical approach, Sivakumar et al.^{27–29} have prepared various magnetic nanoferrites using a highly volatile Fe(CO)₅ as a precursor. Recently, Koltypin et al.³⁰ have described a sonochemical process in which vegetable oils have been used for the synthesis of air stable nanocrystalline iron particles. Looking at the cheap and environment-friendly nature of vegetable oils as compared to the conventional solvents, in the present investigation, we adopt a new route for the preparation of zinc ferrite nanocrystals (4 nm) using simple precursors (without Fe(CO)₅) through ultrasonic emulsification and evaporation.

Emulsions are dispersible liquid–liquid systems, and ultrasound has been proven to be suitable for emulsification and has long been applied.^{31,32} With ultrasound energy, water (dispersed phase) containing the precursor acetates is dispersed in the oil (continuous phase) as small droplets. These droplets are continuously disrupted due to the dissipation of ultrasonic energy. Due to the same energy, the disrupted droplets are stabilized against coalescence. In addition, at the low volume fraction of the dispersed phase used in the present case, chances of mobility and hence coalescence are also reduced considerably. At higher volume fraction of the dispersed phase, smaller droplets after disruption separate more slowly leading to prolonged contact times and a higher probability of coalescence.³³

There are several possible mechanisms of droplet formation and disruption under the influence of ultrasound.^{31–37} One theory suggests the formation of droplets as a consequence of unstable oscillations (capillary waves) of the liquid–liquid interface. These capillary waves may occur and contribute to dispersion only if the diameter of the droplets to be disrupted is sufficiently larger than the wavelength of the capillary waves. For an oil and water system, this wavelength is on the order of 10 μ m. Therefore, in such a system, droplet formation or disruption by capillary waves is unlikely. This has also been concluded by Nedhuzhii,^{34,35} who studied the influence of sound frequency on emulsification. In that case, cavitation should be a viable mechanism responsible for the smaller droplet size of the dispersed phase right after disruption.

Imploding cavitation bubbles cause intensive shock waves in the surrounding liquid and the formation of liquid jets of high liquid velocity. This may cause droplet disruption in the

vicinity of a collapsing bubble. However, the exact process of droplet disruption due to ultrasound, especially as a result of cavitation, is not yet fully understood. Even in the highly viscous liquids, as in the present case, triggering of cavitation is possible as reported by Behrend et al.³³ This is due to evidence that cavitation in the dispersed system is facilitated compared with pure liquids because dispersed particles act as “weak spots” in the system and cavitation will preferably occur at the interface or even inside the water droplets in water and oil (W/O) emulsion.

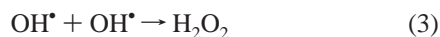
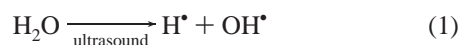
Our present approach is based on sonochemically dispersing an aqueous solution of Zn²⁺ and Fe²⁺ cations into rapeseed oil forming an emulsion of water droplets in oil, without using a surfactant. Again, by ultrasound mediated hydrolysis and oxidation, zinc as well as iron acetates, present in the aqueous droplets, are directly converted to their oxides without any precipitant and without any vigorous calcination. The ultrasonic cavitation events occurring during sonication provide high-temperature conditions or an in situ calcination environment, which facilitates the reaction of sonochemically generated precursors or the oxides for the formation of zinc ferrite nanocrystals. The method, we report here, has the advantage of avoiding the cumbersome conditions that exist in the conventional methods: usage of necessary additive components (stabilizers or surfactants, precipitants) and calcination requirements. In addition, rapeseed oil has replaced organic nonpolar solvents. As is well-known in ferrites, the synthesis route plays a key role in the final properties. For this reason, it is necessary to test new preparation methods and to analyze the effect on the powder characteristics, microstructure of the materials, and, therefore, the magnetic behavior. In view of this point, the synthesized materials obtained by the present strategy have been studied, in detail, for their magnetic properties.

Experimental Section

Materials. The sonochemical strategy was performed using the following powder precursors (analytical grade): Zn(Ac)₂·2H₂O and Fe(Ac)₂ obtained from Wako Pure Chemical Industries Ltd, Japan. Commercial grade rapeseed oil was used. All of these chemicals were used without further purification. For the aqueous phase, double-distilled water was used.

Synthesis. A wide variety of chemical reactions including hydrolysis, oxidation, reduction, dissolution, and decomposition are induced by intense ultrasonic waves and are mainly due to a phenomenon called cavitation.³⁸ Reactions are possible in three different regions of the collapsing bubble generated by ultrasound waves, which are (a) the inner environment of the bubble, where elevated temperatures and pressures are produced causing pyrolysis of water into H and OH radicals, (b) the interfacial region which is between the cavitation bubbles and bulk solution, where temperatures are lower than that of the inner region but still high enough to induce the rupture of chemical bonds, and (c) the bulk of the solution which is at ambient temperature, where the reaction between the reactant molecules and surviving OH or H can still take place.³⁹ Looking at the three regions, in the present case, it seems possible that the reaction occurs in the interfacial region. This is because the metal acetates are ionic, and due to their low vapor pressure, they cannot enter the inner region of the bubble. We believe that the final ferrite could have been formed with the formation of their oxides taking place at first. In this case, the formation of Fe₃O₄ occurs from its acetate, which could be by sonochemical hydrolysis with oxidation, whereas sonochemical hydrolysis alone could be responsible for the formation of ZnO from its

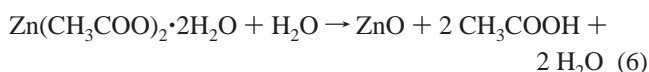
acetate. After the formation of water droplets, we propose the following likely reaction steps for the ultrasonic cavitation mediated formation of ZnFe_2O_4 that occurs in the water droplets:



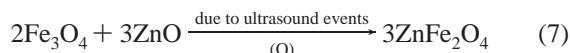
The oxidant generated due to ultrasound cavitation can initiate the oxidation of $\text{Fe}(\text{OH})_2$



In case of zinc acetate, sonochemical hydrolysis could result in the formation of ZnO , as shown in the following equation (6):



Similar ideas have been formulated by Kumar et al.³⁹ and Gutierrez et al.⁴⁰ by studying the sonolysis of nonvolatile solutes such as the acetate anion. After the formation of oxides, high-temperature ultrasonic cavitation events could cause an in situ calcination in order to form the final ferrite as shown below:



Harris et al. have proposed the formation of magnetite nanoparticle ferrofluid and its stabilization using triblock copolymers, but using conventional methods.⁴¹

Characterization. Phase identification was performed by X-ray diffraction (XRD) (RINT – 2500/PC, Rigaku Co. Japan), operating at 50 kV and 30 mA, using $\text{Cu K}\alpha$ radiation in the range of $2\theta = 20\text{--}70^\circ$. Crystallite size and morphology of the as-synthesized and heat-treated ferrites were estimated by transmission electron microscopy (JEOL, JEM-2010 model operating at an accelerating voltage of 200 kV). For this purpose, the nanoferrite samples were deposited on a copper-grid-supported transparent carbon foil. Energy-dispersive X-ray analysis (EDS) was carried out for elemental mapping on a NORAN (Vantage) system, which was operated with an accelerating voltage of 200 keV. Infrared absorption spectra in the $400\text{--}4000 \text{ cm}^{-1}$ frequency range were obtained employing a FT-IR-8400 S (Shimadzu model). In this interferometer is a Michelson type with 30 degree incident angle, dynamic alignment, sealed and desiccated; detector temperature controlled high sensitivity detector (DLATGS Detector); data sampling by He–Ne laser. The window material for FTIR detector is KRS-5 (for wide band). All windows have “wedged” surfaces to prevent unwanted interference effects. Differential thermal and thermogravimetric analysis (DTA/TG) of the as-synthesized ferrite sample was carried out in air using a SDT2960 Thermoanalyzer, utilizing alumina as the reference material, in the temperature range of $30\text{--}1000^\circ\text{C}$ with a heating rate of $10^\circ\text{C}/\text{min}$. Emulsion droplet size was observed using an optical microscope. Magnetic properties of the ferrite nanoparticles were measured employing a SQUID magnetometer (Quantum Design, MPMS-7).

Preparation Procedure. In a typical experiment, 0.176 g of zinc acetate dihydrate, at first, was dissolved into 4 mL of water-

(0.2 M). To this solution was added 0.278 g of iron acetate and dissolved (0.4 M). The thus-generated aqueous solution was then added to 100 mL of rapeseed oil taken in a sonoreactor. The above composition results in an aqueous to oil phase volumetric ratio (W/O) of 1:25. Sonication was then carried out for 20 min in air atm in order to preemulsify the W/O phase, maintaining the temperature between 25 and 30°C using a cooling bath. Sonication was applied using an ultrasonic probe with a 1/2 in. ($\sim 1.27 \text{ cm}$) titanium tip (Branson Digital Sonifier, model 450, Branson Ultrasonics Corporation, Danbury). The frequency and power applied were 20 kHz and 70 W, respectively. The probe tip was kept at 5 mm from the top of the oil surface. Initially, with the application of ultrasound, the two distinct layers were changed to a uniformly turbid emulsion, within 5 min. After 20 min of preemulsification, sonication was continued further for 30 min without cooling in order to initiate the hydrolysis and oxidation of zinc and iron acetates as well as an in situ calcination of the formed oxides. In the absence of cooling, the temperature increased rapidly due to the continuous dissipation of ultrasonic energy in the liquid. In both of the above cases, sonication was carried out in a pulse on/off mode (9 s on and 3 s off).

At the end of 30 min of sonication, the temperature of the reaction reached 125°C ; thus, all of the water present in the internal aqueous droplets evaporated leaving behind the solid particles dispersed in the oil phase. Separation of the brown solid particles from the oil phase was achieved by centrifuging the suspension at 5000 rpm for 1 h. After decanting the oil phase, the solid particles were then washed 3 times with ethanol in order to remove the small amounts of oil that may be present on the surface of the solid product. Finally, the obtained solid product was dried under vacuum at room temperature. Heat treatment of the as-synthesized ferrite sample was carried out at 350°C for 3 h, applying a heating rate of $5^\circ\text{C}/\text{min}$ in air atm. The yield of the above ultrasonic preparation was then calculated which was quantitative and as high as 98%. A small loss in the product may occur during the washing stage of the product with ethanol. The typical process followed has been depicted in Figure 1.

Results and Discussion

(A) DTA and TG. DTA and TG data (recorded from room temperature to 1000°C) of the as-synthesized ferrite sample are shown in Figure 2. The DTA pattern shows a small endothermic transformation between room temperature and 80°C . This endothermic peak is accompanied by a weight loss of $\approx 11\%$ in the TG curve. This can be attributed to the loss of a small quantity of ethanol that is adsorbed on the solid surface of the as-synthesized sample, which has not been removed even after room temperature vacuum-drying. As shown by XRD and TEM in the following discussion, the as-synthesized sample is a small particle powder. Thus, a high degree of adsorption of ethanol molecules and other substances probably occurs on the surface. A strong exothermic peak centered at 350°C in DTA accompanied by a weight loss of $\approx 14\%$ in the TG curve could also be observed.

The possible presence of a small amount of oil that has been adsorbed and was not removed from the surface even after washing with ethanol could contribute to both the weight loss in the TGA and the exothermic process in the DTA in the abovementioned temperature range. In our case, DTA-TG as well as the heat treatment of the as-synthesized sample was carried out in the presence of air atm and we believe that oil combustion (decomposition) might result in a strong exothermic peak at about 350°C .

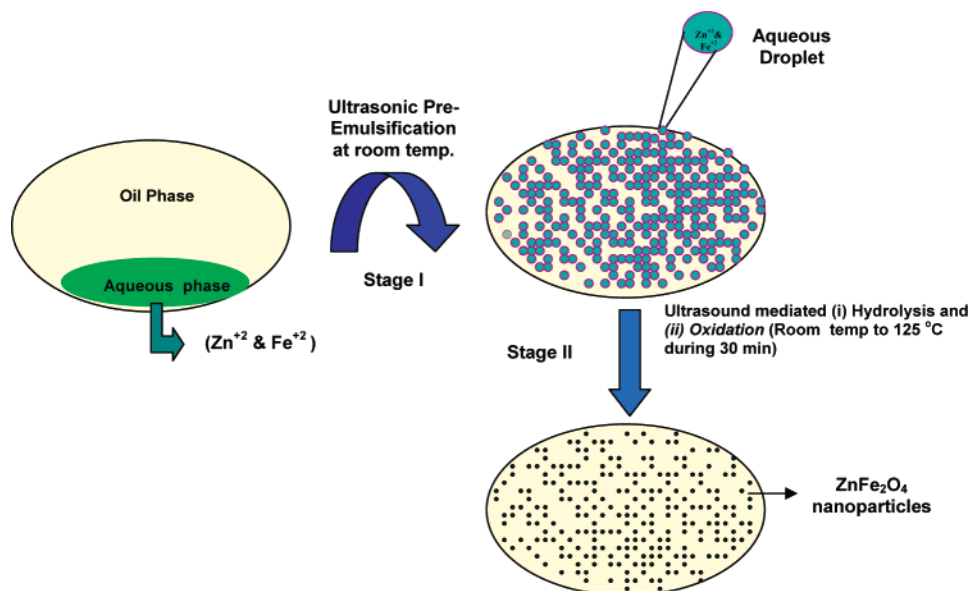


Figure 1. Schematic representation of ultrasonic cavitation method for the preparation of nanoparticles of ZnFe₂O₄.

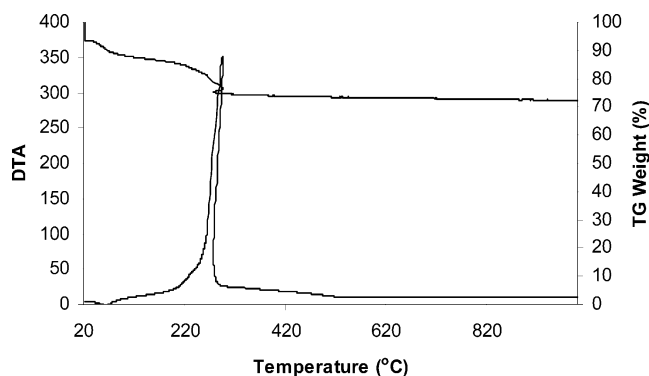


Figure 2. DTA/TG of the sonochemically as-synthesized ZnFe₂O₄ obtained at a heating rate of 10 °C/min.

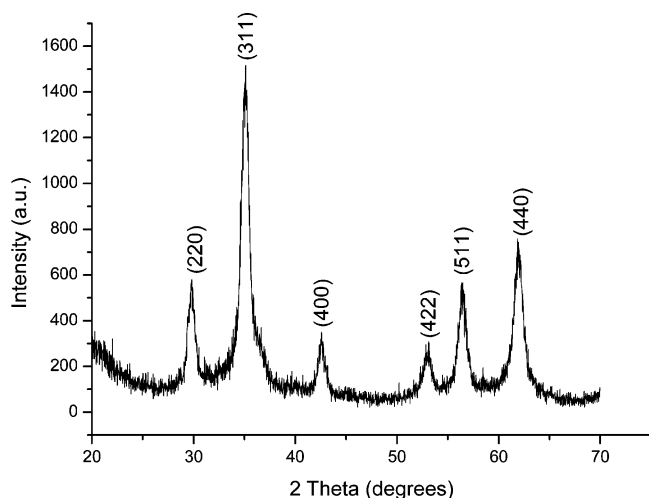


Figure 3. X-ray powder diffractogram of zinc ferrite nanoparticles. The characteristic diffracted directions (220), (311), (400), (422), (511), and (440) of the spinel structure are indexed.

(B) XRD. Crystalline phase characterization is carried out using XRD pattern. Well-defined and broader diffraction peaks, all corresponding to characteristic crystallographic planes like (220), (311), (400), (422), (511), and (440) of the spinel structure⁴² can be observed in Figure 3. All of the recorded diffraction peaks are well-assigned to the structure of standard polycrystalline ZnFe₂O₄ (Franklinite, JCPDS 22-1012). Broad-

TABLE 1: Comparison of Standard and Experimental Peak Intensity Values for Zinc Ferrite with Their Respective Diffraction (*hkl*) Planes

<i>hkl</i>	<i>d_{hkl}</i> (Å)	<i>I_{exp}</i>	<i>I_{ASTM}</i>	<i>hkl</i>	<i>d_{hkl}</i> (Å)	<i>I_{exp}</i>	<i>I_{ASTM}</i>
220	2.903	35.45	30	422	1.697	16.38	12
311	2.508	100	100	511	1.609	35.45	30
400	2.080	18.06	17	440	1.479	60.6	60

ening of the peaks exhibited the nanocrystalline nature of the sample. The mean crystallite size was estimated to be 4 nm from the half-maximum full width of the (311) peak by the modified Scherrer formula.⁴³ FWHM value for instrumental broadening was carried out by running the reference sample (Silicon). This value was then subtracted from the observed value of the sample. Also, the values have been checked for other major lines, and it matches with the value what we have reported here. In addition, the X-ray diffraction patterns of the heat treated ferrite at 350 °C for 3 h were also collected, and no significant variation was found compared to those of as-synthesized sample.

Table 1 shows the crystallographic analysis of ZnFe₂O₄ nanoparticles. The interplanar spacing *d_{hkl}* is calculated from the line position by using the Bragg law. The experimental peak intensities *I_{exp}* are compared to the ASTM ones (ASTM no. 22–1012 (ZnFe₂O₄)). It can be observed that the experimental peak intensity values are in close agreement with the standard values for the respective diffraction (*hkl*) planes.

(C) TEM. Additionally from TEM observations, as shown in Figure 4A–D, one can see that there is no significant difference in the morphology between the as-synthesized and heat-treated ferrite at 350 °C for 3 h except that the size of the heat treated ferrite has increased to ~12 nm as compared to the as-synthesized ferrite size of ~4 nm. We can also observe that the zinc ferrite phase occurs as more or less spherical particles in both the cases. As shown in the inset of Figure 4A, the well-defined rings in the SAD pattern can be assigned to the crystal planes of the ZnFe₂O₄ phase, indicating the established crystallinity of the ZnFe₂O₄ particles. Figure 4A,B again confirms the formation of crystalline ZnFe₂O₄ in the as-synthesized sample itself.

(D) IR. IR spectra of rapeseed oil as well as the emulsion formed due to ultrasound irradiation of oil and water for comparison purposes have been shown in Figure 5a. Both the

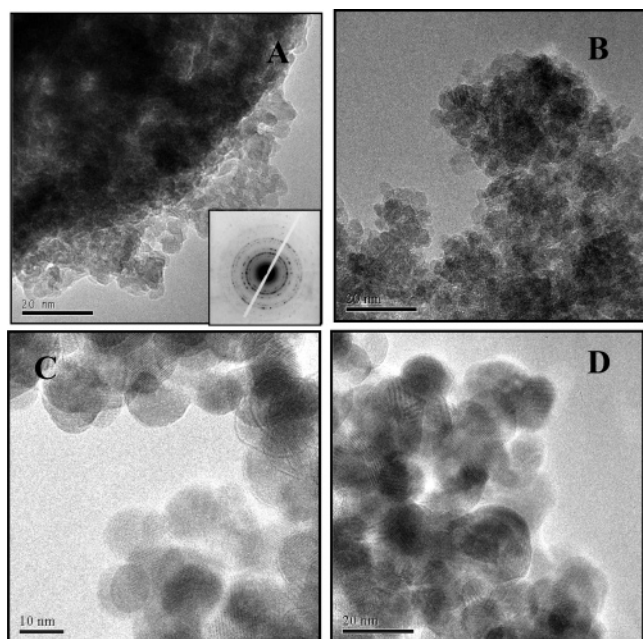


Figure 4. TEM micrographs of as-synthesized (A and B) and heat-treated (C and D) zinc ferrite nanocrystals. Inset of A shows the electron diffraction (ED) pattern of as-synthesized zinc ferrite nanocrystals.

spectrum show characteristic bands appearing at 2930 and 2850 cm^{-1} which are characteristic of C–H asymmetric and symmetric stretching vibrations, respectively, due to the $-\text{CH}_2-$ groups of the long aliphatic alkyl groups. The peak at 2366 cm^{-1} arises due to CO_2 . The two dominant peaks appearing at 1752 and 1467 cm^{-1} are ascribed to the $\text{C}=\text{O}$ stretching and $\text{H}-\text{C}-\text{H}$ bending vibrations, respectively. Also, the peak at 1169 cm^{-1} arises due to C–O stretching vibration.⁴⁴ On the other hand, the IR spectrum of the as-synthesized ferrite sample, as shown in Figure 5b, indicates a typical absorption band for the spinel structure of the ferrite at 564 cm^{-1} , in addition to the characteristic bands, as shown by oil or oil–water emulsion in Figure 5a. The existence of a band around the 560 cm^{-1} band strongly suggests the Fe–O stretching vibration (γ_1 mode).⁴⁵ The IR spectrum of the heat-treated sample has been shown in Figure 5c which reveals only the characteristic band of the ferrite appearing at 564 cm^{-1} , leaving behind other peaks characteristic of oil as shown in Figure 5a,b. All of these further demonstrate that the crystalline ferrite is formed in the as-synthesized sample itself with the contamination of a small amount of oil, which has been removed by carrying out heat treatment at 350 °C for 3 h.

(E) EDS. To confirm the chemical composition of the as-synthesized ferrite, EDS spectra were recorded at a number of positions of the product during TEM imaging, and a representative spectrum has been shown in Figure 6. The chemical signatures obtained are identical within experimental accuracy and essentially only Zn, Fe, and O elements are observed with the expected stoichiometric proportions for ZnFe_2O_4 . This further confirms the formation of ferrite crystallites in the as-synthesized sample. The presence of Cu signal within the spectrum arises from the mesh grid supporting the lacey carbon film. The EDS for the heat-treated sample also exhibits a very similar composition and spectrum as that of as-synthesized ferrite sample.

All of these XRD, TEM, IR, and EDS studies clearly demonstrate that the as-synthesized material obtained by the present sonochemical protocol were indeed nanoparticles of crystalline ZnFe_2O_4 ferrite.

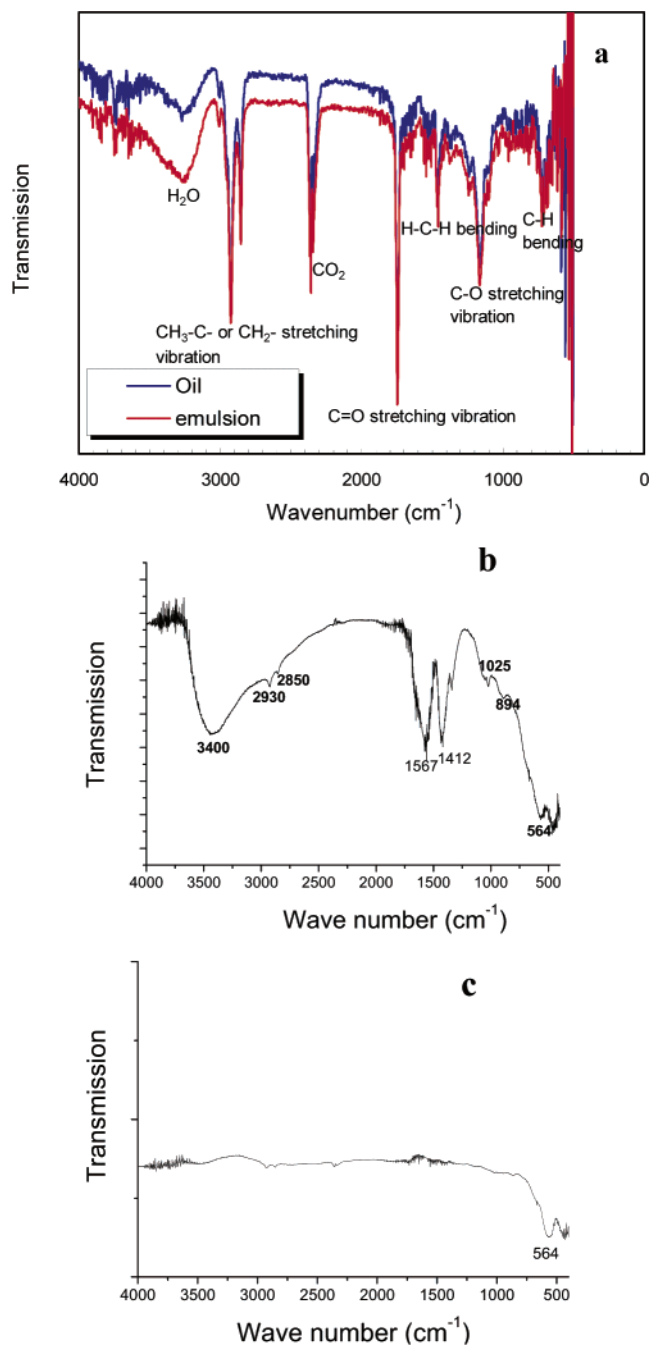


Figure 5. Typical IR-absorption spectra obtained for (a) rapeseed oil and emulsion for comparison and ZnFe_2O_4 ferrite nanoparticles by the sonochemical method, (b) as-synthesized and (c) heat-treated sample.

(F) Magnetic Properties of Nanocrystalline ZnFe_2O_4 Prepared at Room Temperature and Heat Treated at ~ 350 °C. Detailed magnetic measurements, zero-field cooled (ZFC) and field cooled (FC) magnetization vs temperature under different fields, magnetic hysteresis loops at several temperatures, magnetic relaxation at different temperatures and under different fields have been carried out in order to study the magnetic properties of the as-synthesized and calcined powders.

In Figure 7, we show the hysteresis loops, measured at different temperatures, for the as-synthesized ZnFe_2O_4 . At low field, the patterns depict hysteresis with finite coercivity and a tendency of saturation whereas at high field the magnetization tends to increase almost linearly reflecting antiferro or paramagnetic behavior. The entire pattern is similar to what has

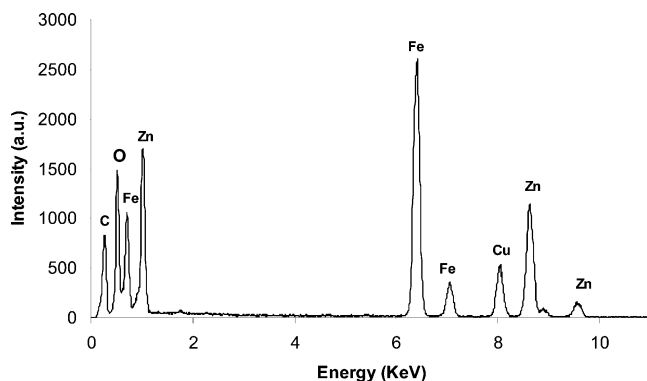


Figure 6. Representative EDS spectrum of the as-synthesized ferrite.

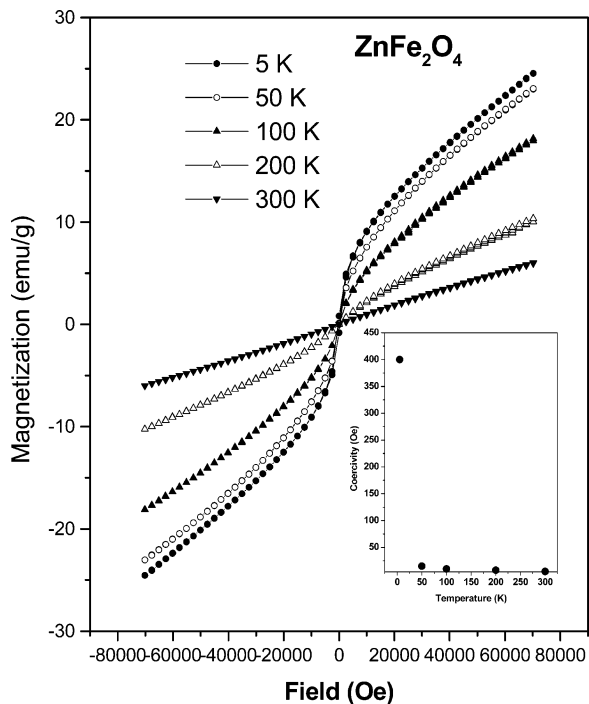


Figure 7. Hysteresis loops measured at different temperatures for the as-synthesized ferrite. Inset shows the variation of coercivity (H_c) with temperature (K).

been observed by others^{1,11–15} in nanocrystalline ZnFe₂O₄. In the inset of Figure 7, we show the variation of coercivity (H_c) with temperature. The magnetization at maximum field (M_s) varies over ~ 5 – 25 emu/g from room temperature down to ~ 5 K. The reason behind difference between the M_s values observed in bulk and nano-systems could be increased cation disorder and/or surface effects in nano-system.

Figure 8 shows the variation of magnetization with temperature, both under zfc and fc conditions, under 5000 and 70 000 Oe fields, respectively. It is interesting to note that the curves diverge below a certain temperature. This point could either mark the blocking temperature (T_B) or a spin glass transition temperature.⁴⁶ The temperature appears to be increasing with field: from ~ 15 K under 5000 Oe to ~ 75 K under 70 000 Oe, i.e., a field-dependent $T_B(H)$.¹¹ It is also noteworthy that the degree of divergence between zfc and fc magnetization data increases with the increase in applied field. In the case of finer particles having sizes less than the size of a single domain, one observes superparamagnetism above T_B . Under higher field, the correlation length of the magnetic order seems to grow which, in turn, gives rise to a shift in T_B toward a higher value. In the absence of sufficient high-temperature data, Curie–Weiss fitting

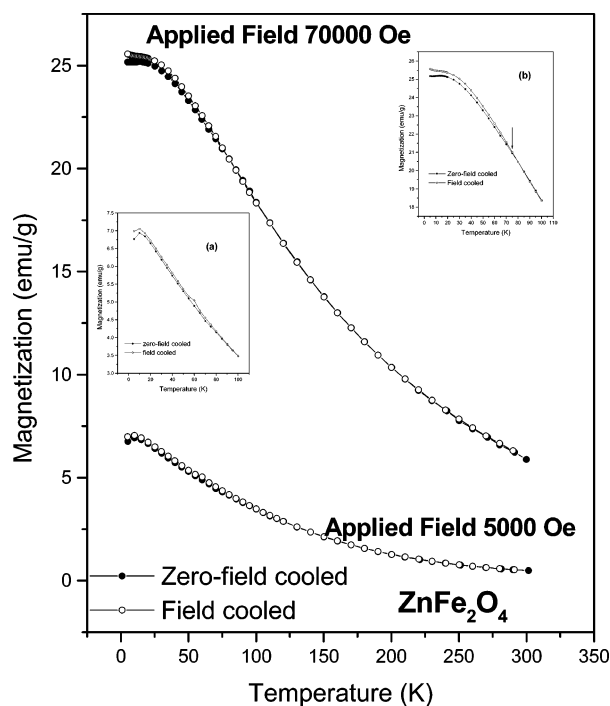


Figure 8. Variation of magnetization with temperature both under zfc and fc conditions and under 5000 and 70 000 Oe field. Inset (a) shows the enlarged view to indicate the blocking temperature to be ~ 15 K at 5000 Oe field and (b) shows the enlarged view to indicate the blocking temperature to be ~ 75 K under 70 000 Oe field.

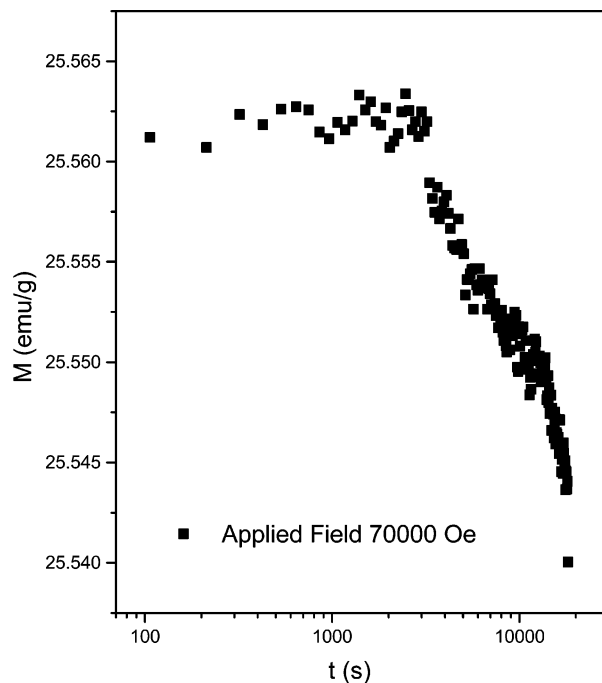


Figure 9. Relaxation pattern of the magnetization (M) at ~ 5 K (i.e., below T_B) and under ~ 70 000 Oe.

could not be done. Comparison of the hysteresis loops in Figure 7 and zfc/fc magnetization patterns under different fields in Figure 8 reveals an interesting “history”-dependence of the magnetization below $T_B(H)$. The “history”-dependence, in turn, depends on whether a field-sweep or a temperature-sweep protocol is used. For instance, comparison of hysteresis loop at ~ 5 K with the zfc/fc data under ~ 5000 Oe at ~ 5 K reveals that under zfc condition the field-sweep protocol (which is used when the hysteresis loop is traced) does not give rise to sizable

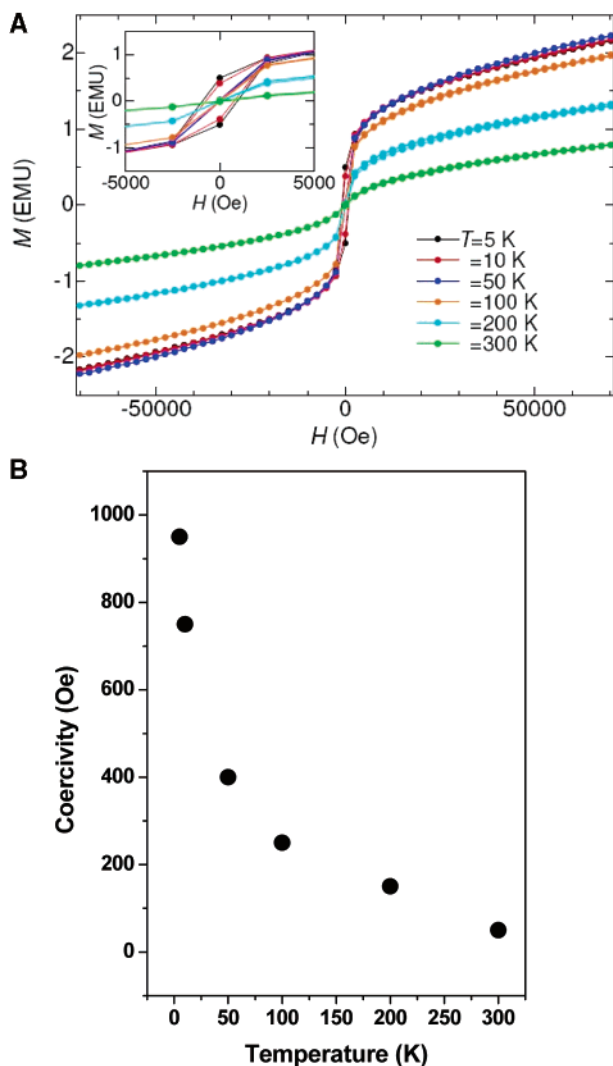


Figure 10. (A) Hysteresis loops measured at different temperatures over 5–300 K for the heat-treated ferrite sample; (B) Variation of coercivity (H_c) with temperature (K) for the heat-treated ferrite sample.

“history” dependence. In other words, the magnetization under both ascending and descending branch turns out to be nearly identical at ~ 5000 Oe and ~ 5 K. On the other hand, the temperature-sweep protocol reveals sizable “history”-dependence even under ~ 5000 Oe.

Therefore, the zfc hysteresis loop and zfc/fc magnetization vs temperature pattern at ~ 5 K and under ~ 5000 Oe do not measure the same state of magnetization at ~ 5 K and under ~ 5000 Oe. Nearly reversible magnetization within ~ 1000 – $70\,000$ Oe, during hysteresis loop tracing, gives way to sizable irreversibility under zfc/fc temperature sweep. This discrepancy between field and temperature sweep is quite prominent only below $T_B(H)$. Above $T_B(H)$, all of the magnetization patterns are found to be reversible. This behavior is quite unusual and detailed investigation on the “history”-dependence of magnetization below $T_B(H)$ under both field-sweep and temperature-sweep protocol will be attempted in nanoscale ferrites in near future.

In Figure 9, we show the relaxation pattern of the magnetization (M) at ~ 5 K (i.e., below T_B) and under $\sim 70\,000$ Oe. Interestingly, there are three different regimes of relaxation: below ~ 3000 s, there is virtually no relaxation, between ~ 3000 – $13\,000$ s, the magnetization drops logarithmically with time and, finally, between $13\,000$ and $20\,000$ s, the rate of relaxation increases further while maintaining the logarithmic

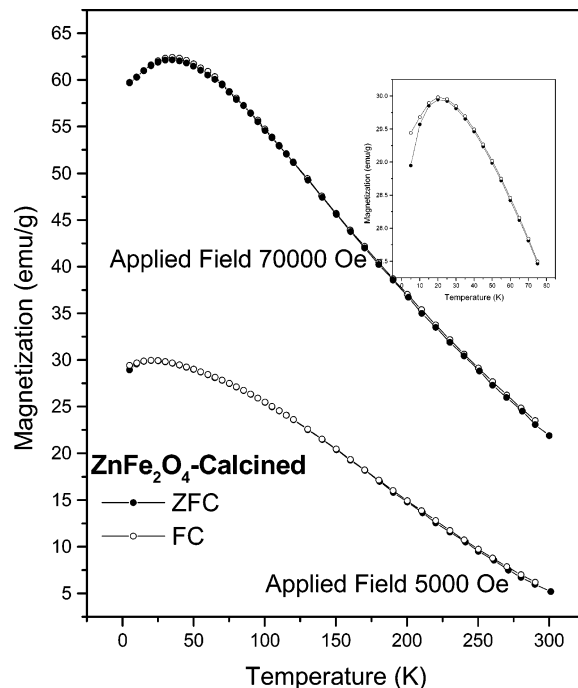


Figure 11. Variation of magnetization with temperature both under zfc and fc conditions and under 5000 and 70 000 Oe field. Inset shows the enlarged view to indicate the divergence at ~ 75 K under 5000 Oe field.

time dependence. In a metastable system, spin glass relaxes following a different pattern from a system with long-range order. A strongly interacting system exhibits slower magnetic relaxation of the form $M(t) = M_0 e^{-(t/\tau)^\beta}$, $0 < \beta < 1$, which may give way to a simple Debye form with $\beta = 1$ for more conventional magnetic order having single activation energy. In many cases, the relaxation activation energies are spatially distributed, and as a result, the relaxation times are also distributed. In those cases, the relaxation pattern can be approximated as logarithmic $M(t) = M_0 + S \ln(t)$, where S is the magnetic viscosity. The relaxation normally occurs because of domain-wall movement, magnetic moment rotation, or nucleation of reverse magnetization. In our case, it seems that the relaxation follows standard flux creep pattern where magnetization (M) is given by $M = M_0 [1 - (k_B T/E) \ln(t/\tau)]$; M_0 is the magnetization at $t = 0$, E is the characteristic activation energy, and τ is a characteristic time scale for relaxation. The creeping could be related to defect activation, which in turn gives rise to relaxation in domain-wall pinning. We estimated the activation energy across the time scale, over which there is relaxation in magnetization, by noting the corresponding rate of relaxation $S = dM/d \ln t$. S turns out to be -0.01496 between ~ 3000 and $13\,000$ s and -0.04499 between ~ 13000 and $20\,000$ s. Therefore, between ~ 3000 and $13\,000$ s, E is found to be 0.735 eV, whereas between $13\,000$ and $20\,000$ s, E is 0.244 eV. It has been shown⁴⁷ that for an ordered magnetic system S is given by $S = k_B T / a \nu M_s$, where a is a constant which depends on the thermal activation process and ν is the activation volume. Since $\nu(t)$ depends on time t and, as time passes, less and less volume relaxes due to a smaller effect of thermal activation, S turns out to be larger. As a result, E becomes smaller. We have compared these results with the results obtained in the case of the heat-treated sample at 350 °C. For this purpose, the as-synthesized nanocrystalline ZnFe₂O₄ is heat treated at ~ 350 °C, and detailed magnetic measurements have been carried out on this sample. In Figure 10A, we show the hysteresis loops measured at different temperatures over 5–300 K. Although,

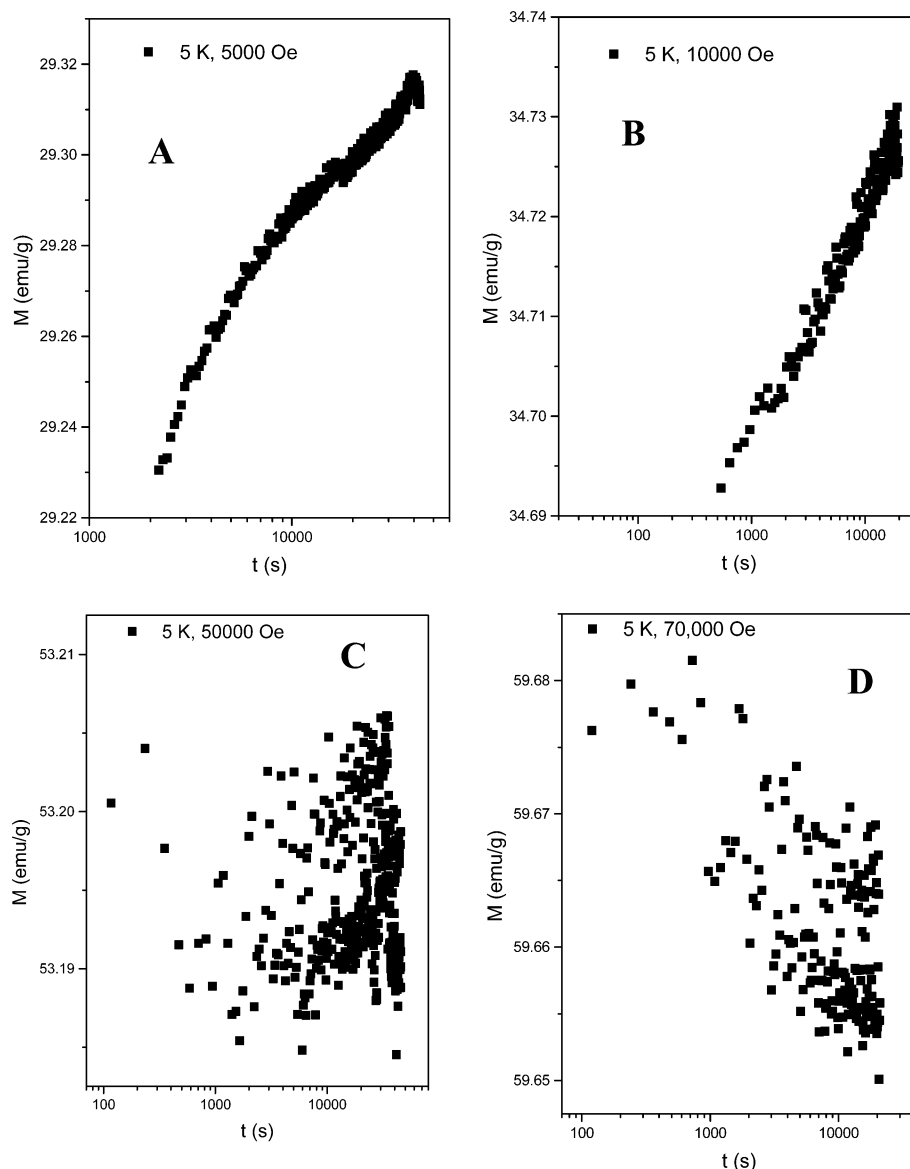


Figure 12. Relaxation patterns at 5 K under fields of 5000, 10 000, 50 000, and 70 000 Oe, respectively.

the pattern of the hysteresis loop remains more or less same, reflecting two different magnetic phases, the magnetization at the maximum field (M_s) appears to be higher than that observed in the case of the as-synthesized sample. M_s varies over 17–56 emu/g between room temperature down to ~5 K. The coercivity (H_c) also has increased quite a bit. H_c is found to be ~950 Oe at ~5 K and ~50 Oe at 300 K. Figure 10B shows the variation of H_c with temperature.

In Figure 11, we show the magnetization vs temperature, under zero-field cooled and field cooled conditions under 5000 and 70 000 Oe fields. Interestingly, although the patterns diverge at around ~15 K under a field 5000 Oe, they merge completely across the temperature range 5–300 K under higher field (70 000 Oe). This is quite a contrast in comparison to the behavior observed in the as-synthesized sample. This could be because with calcination the particle size grows which gives rise to a stable magnetic order as opposed to metastable glassy/frustrated and/or superparamagnetic behavior. As a result, under higher field, one observes no divergence between zfc and fc curves. Here too, in the absence of high-temperature data, we could not perform the Curie–Weiss fitting.

Finally, in Figure 12A–D, we show the relaxation patterns at 5 K under different fields of 5000, 10 000, 50 000, and 70 000 Oe, respectively. The patterns, interestingly, depend on field as well as on time, especially at low field. At low field (5000 Oe), it seems the domain rotation is not complete, and therefore, the magnetization increases with time following different rates across different time interval. However, it is noteworthy that in all of the cases logarithmic time dependence is maintained. By noting the relaxation rate S corresponding to a particular time interval, we evaluated the activation energies (E). E is found to be ~0.088 eV corresponding to a time period of ~2000–3300 s, ~0.156 eV corresponding to ~3300–7000 s, and ~0.273 eV corresponding to ~7000–43 000 s. The activation volume v in this case increases with time giving rise to a drop in S and a rise in E . At 10 000 Oe, the magnetization still depicts an increase with time with an activation energy of ~0.641 eV over a time period of ~500–20 000 s. At 50 000 Oe, the magnetization remains virtually constant with no relaxation. Finally, at even higher field (70 000 Oe), the magnetization drops with time with an activation energy of ~2.624 eV over a time period of 100–20 000 s. Therefore, it is quite clear that at 5 K under low field the magnetization process was not complete, and it

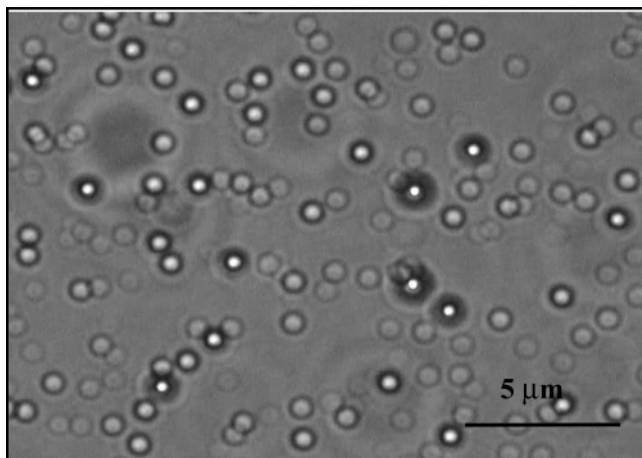


Figure 13. Emulsion droplets observed by optical microscope

continues over a long time scale ($\sim 40\,000$ s) though slows down with time. Once the saturation is reached, because of flux creeping, the magnetization starts decreasing with time. It is interesting to point out that the relaxation rate at higher field is higher for the as-synthesized sample, reflecting the metastable state even at low temperature, than that for the heat-treated sample.

(G) Formation Mechanism of Crystalline Nanoparticles of Zinc Ferrite. Highly homogeneous, small, and uniform sized ferrite particles obtained in this process seem feasible due to the generation of efficient emulsion droplets induced by ultrasound. Figure 13 shows the representative light microscope picture of the emulsion droplets. From this figure, it can be seen that the average size of the droplets is about $0.421\ \mu\text{m}$. To confirm the absence of coalescing of the droplets even at high temperature, the size of the droplets prior to evaporation was also checked, which is about $0.456\ \mu\text{m}$. The volume drop size distribution study carried out by Abismail et al.³¹ clearly indicates that even for low ultrasound power values (after 30 s with a power of 30 W) the size of the droplets goes down from 100 to $0.7\ \mu\text{m}$. In our case, the size of the droplets after 30 min of ultrasound application was about $0.421\ \mu\text{m}$.

To confirm whether the formed individual emulsion droplets acted as microreactors to form an individual ferrite particle, the sizes of the resultant ferrite particle diameters were compared to the original emulsion droplet diameter. The emulsion droplets formed in our case are in the size range of $0.421\ \mu\text{m}$ (as observed by optical microscope), whereas the size of the crystallites formed are of 4 nm (as observed from TEM). This indicates that there is a good probability of formation of a large number of nuclei of ferrite from each droplet.

Conclusion

In summary, a facile route of an ultrasound-assisted emulsification and evaporation process is successfully demonstrated for the synthesis of nanocrystalline zinc ferrite with narrow size distribution. Utilization of this method results in the formation of much finer particles with an average diameter of ~ 4 nm in the case of as-synthesized ferrite and ~ 12 nm for the heat-treated ferrite sample. It is noteworthy that this method has the advantage of avoiding the cumbersome conditions that exists in the conventional methods; usage of necessary additive components (stabilizers or surfactants, precipitants) and calcination requirements. In addition, rapeseed oil has replaced organic nonpolar solvents used in earlier studies.

The sonochemically as-synthesized nanocrystalline ZnFe_2O_4 system depicts greater metastability even at low temperature

and under higher field, as expected. The heat-treated nanocrystalline sample depicts higher magnetization and decreased metastability. Under high field, there is no signature of spin order metastability in the magnetization vs temperature plot. The values of the magnetization and coercivity at different temperatures tally with the reported results. In addition, we also observe the relaxation of the magnetization in both the as-synthesized and heat-treated samples. In the case of the as-synthesized sample, it is quite likely that superparamagnetism sets in above T_B . As a result of that, H_c tends to almost zero above T_B . The relaxation rate S is also quite high even at a lower temperature (~ 5 K) and under higher field ($\sim 70\,000$ Oe) because of temperature-dependent fluctuations in small particles.

It has been shown earlier¹² with the help of extended X-ray absorption fine structure (EXAFS) study that, as the particles become finer, occupancy at A and B sites varies, and as a result, a disordered structure develops which gives rise to higher magnetization compared to that of bulk ceramic. A higher magnetization for the as-synthesized ZnFe_2O_4 system and even higher magnetization for the heat-treated sample observed can be interpreted as due to variation in temperature-dependent fluctuation effects (thermal activation), whereas the disorder effect is present in both of the systems. Because of superparamagnetism above T_B , fluctuation remains stronger even at lower temperatures, S is 2 orders of magnitude higher, in the as-synthesized sample. On the other hand, for the heat-treated sample, the divergence point between fc and zfc curves can be interpreted as the onset of the spin glass/metastable state with smaller fluctuation. The fluctuation rate S under the same conditions is lower. Therefore, it appears one can tailor the magnetization and its relaxation behavior by suitably preparing nanocrystalline ZnFe_2O_4 followed by appropriate heat treatment. Furthermore, these findings are very important because, given the general success of this developed sonochemical approach, it can be anticipated undoubtedly that this method should be able to be used as a prototype reaction for the synthesis of various other ferrites.

Acknowledgment. The authors thank the JSPS Postdoctoral Fellowship program for foreign researchers as well as NEDO of Japan for financial support of this research.

References and Notes

- (1) Caruntu, G.; Bush, G. G.; O'Connor, C. J. *J. Mater. Chem.* **2004**, *14*, 2753.
- (2) Kamazawa, K.; Tsunoda, Y.; Odaka, K.; Kohn, K. *J. Phys. Chem. Solids* **1999**, *60*, 1261.
- (3) Tung, L. D.; Kolesnichenko, V.; Caruntu, G.; Caruntu, D. *Physica B* **2002**, *319*, 116.
- (4) Chu, X.; Liu, X.; Meng, G. *Sens. Actuators B* **1999**, *55*, 19.
- (5) Valenzuela, M. A.; Bosch, P.; Jimenea, J.; Quiroz, O. *J. Photochem. Photobiol. A* **2002**, *148*, 177.
- (6) Steinike, U.; Tkacova, K. *J. Mater. Syn. Process.* **2000**, *8*, 199.
- (7) Zhuiykov, S.; Ono, T.; Yamazoe, N.; Miura, N. *Solid State Ionics* **2002**, *152/153*, 801.
- (8) Schiessl, W.; Potzel, W.; Karzel, H.; Steiner, M.; Kalvius, G. M.; Martin, A.; Krause, M. K.; Halevy, I.; Gal, J.; Schafer, W.; Will, G.; Hillberg, M.; Wappling, R. *Phys. Rev. B* **1996**, *53*, 9143.
- (9) Morrison, S. A.; Cahill, C. L.; Carpenter, E. E.; Calvin, S.; Swaminathan, R.; McHenry, M. E.; Harris, V. G. *J. Appl. Phys.* **2004**, *95*, 6392.
- (10) Skomski, R. *J. Phys.: Condens. Matter* **2003**, *15*, R841.
- (11) Hocheppied, J. F.; Bonville, P.; Pileni, M. P. *J. Phys. Chem. B* **2000**, *104*, 905.
- (12) Jeyadevan, B.; Tohji, K.; Nakatsuka, K. *J. Appl. Phys.* **1994**, *76*, 6325.
- (13) Yokoyama, M.; Oku, T.; Taniyama, T.; Sata, T.; Ohta, E.; Sato, T.; Haneda, K.; Itoh, S.; Kurahashi, K.; Takeda, M. *Physica B* **1995**, *213–214*, 251.

- (14) Grasset, F.; Labhsetwar, N.; Li, D.; Park, D. C.; Saito, N.; Haneda, H.; Cador, O.; Roisnel, T.; Mornet, S.; Duguet, E.; Portier, J.; Etourneau, J. *Langmuir* **2002**, *18*, 8209.
- (15) Zhou, Z. H.; Wang, J.; Xue, J. M.; Chan, H. S. O. *J. Mater. Chem.* **2001**, *11*, 3110.
- (16) Jiao, Z.; Li, M.; Bian, L.; Liu, J. *J. Inorg. Mater.* **2001**, *17*, 631.
- (17) Martin de Vidales, J. L.; López-Delgado, A.; Vila, E. *J. Alloys Compd.* **1999**, *287*, 276.
- (18) Chen, N.; Yang, X.; Liu, E.; Huang, J. *Sens. Actuators B* **2000**, *66*, 178.
- (19) Yuan, Z.; Zhang, L. *Mater. Res. Bull.* **1998**, *33*, 1587.
- (20) Jin, J.; Bai, T.; Chang, X.; Bai, B. *Chem. Res. Appl.* **2001**, *13*, 667.
- (21) Yu, S.; Fujino, T.; Yoshimura, M. *J. Magn. Magn. Mater.* **2003**, *256*, 420.
- (22) Toledo, J. A.; Valenzuela, M. A.; Bosch, P.; Armendáriz, H. *Appl. Catal. A* **2000**, *198*, 235.
- (23) Mohai, I.; Szépvölgyi, J.; Bertóti, I.; Mohai, M. *Solid State Ionics* **2001**, *141/142*, 163.
- (24) Yang, H.; Zhang, X.; Huang, C.; Yang, W.; Qiu, G. *J. Phys. Chem. Solids* **2004**, *65*, 1329.
- (25) Shafi, K. V. P. M.; Ulman, A.; Lai, J.; Yang, N.-L.; Cui, M.-H. *J. Am. Chem. Soc.* **2003**, *125*, 4010.
- (26) Cahn, R. W. *Encyclopedia of Materials science and Engineering*; Pergamon Press: Oxford, 1993.
- (27) Sivakumar, M.; Gedanken, A.; Zhong, W.; Du, Y. W.; Bhattacharya, D.; Yeshurun, Y.; Felner, A. *J. Magn. Magn. Mater.* **2004**, *268* (1–2), 95.
- (28) Sivakumar, M.; Gedanken, A.; Zhong, W.; Du, Y. W.; Bhattacharya, D.; Bruckental I.; Yeshurun Y.; Felner, I. *J. Mater. Chem.* **2004**, *14* (4), 764.
- (29) Sivakumar, M.; Gedanken, A.; Zhong, W.; Jiang, H. Y.; Du, Y. W.; Bhattacharya, D.; Bruckental, I.; Yeshurun, Y.; Felner, A. *Chem. Mater.* **2004**, *16*, 3623.
- (30) Koltypin, Y.; Perkas, N.; Gedanken, A. *J. Mater. Chem.* **2004**, *14*, 2975.
- (31) Abismaïl, B.; Canselier, J. P.; Wilhelm, A. M.; Delmas, H.; Gourdon, C. *Ultrason. Sonochem.* **1999**, *6* (1–2), 75.
- (32) Abismaïl, B.; Canselier, J. P.; Wilhelm, A. M.; Delmas, H.; Gourdon, C. *Ultrason. Sonochem.* **2000**, *7* (4), 187.
- (33) Behrend, O.; Ax, K.; Schubert, H. *Ultrason. Sonochem.* **2000**, *7* (2), 77.
- (34) Neduzhii, S. A. *Soviet Phys./Acoust.* **1962**, *8*, 378.
- (35) Neduzhii, S. A. *Soviet Phys./Acoust.* **1965**, *10*, 390.
- (36) Li, M. K.; Fogler, H. S. *J. Fluid Mech.* **1978**, *88*, 499.
- (37) Li, M. K.; Fogler, H. S. *J. Fluid Mech.* **1978**, *88*, 513.
- (38) Suslick, K. S. *Ultrasound: Its Chemical, Physical and Biological effects*; VCH: Weinheim, Germany, 1988.
- (39) Kumar, R. V.; Diamant, Y.; Gedanken, A. *Chem. Mater.* **2000**, *12*, 2301.
- (40) Gutierrez, M.; Henglein, A.; Fisher, C. H. *Int. J. Radiat. Biol.* **1986**, *50*(2), 313.
- (41) Harris, L. A.; Goff, J. D.; Carmichael, A. Y.; Riffle, J. S.; Harburn, J. J.; St. Pierre, T. G.; Saunders, M. *Chem. Mater.* **2003**, *15*, 1367.
- (42) *International Tables for X-ray Crystallography*; Kynoch Press: Birmingham, England, 1968.
- (43) Klug, H. P.; Alexander, L. E. *X-ray Diffraction Procedure for Polycrystalline and Amorphous Materials*; Wiley: New York, 1974.
- (44) *Interpretation of Infrared Spectra: A Guide to the Complete Interpretation of Infrared Spectra of Organic Structures*; Roeges, N. P. G., Ed.; J. Wiley & Sons: Chichester, U.K., 1993.
- (45) Rao, G. V. S.; Rao, C. N. R.; Ferraro, J. R. *Appl. Spectrosc.* **1970**, *24*, 436.
- (46) Cador, O.; Grasset, F.; Haneda, H.; Etourneau, J. *J. Magn. Magn. Mater.* **2004**, *268*, 232.
- (47) Gaunt, P. J. *J. Appl. Phys.* **1986**, *59*, 4129.